Mechanistic investigation of silicon-graphite/$LiNi_{0.8}Mn_{0.1}Co_{0.1}O_2$ commercial cells for non-intrusive diagnosis and prognosis

Research paper

(Revised Version)

D. Anseán[1,*], G. Baure[2], M. González[1], I. Cameán[3], A.B. García[3], and M. Dubarry[2,*]

[1] Department of Electrical Engineering, Polytechnic School of Engineering, University of Oviedo, 33204, Gijón, Asturias, Spain

[2] Hawai'i Natural Energy Institute, University of Hawai'i at Mānoa, 1680 East-West Road, POST 109, Honolulu, HI 96822, USA

[3] Instituto Nacional del Carbón (CSIC), Francisco Pintado Fe 26, 33011, Oviedo, Asturias, Spain

*Corresponding authors

David Anseán

Tel.: +34 985 182 556; fax: +34 985 182 138.

E-mail address: anseandavid@uniovi.es

Matthieu Dubarry

Tel.: +1 808 956 2349; fax: +1 808 956 2336.

E-mail address: matthieu@hawaii.edu

Abstract

Due to their high energy density, lithium-ion batteries with blended silicon-graphite (Si-Gr) anodes and nickel-rich (NMC) cathodes have been regarded as one of the most promising technologies for next-generation consumer electronics and electric vehicles. However, there are still several technical challenges to overcome for successful wide-spread adoption; in particular, deciphering the degradation phenomena remains complex and challenging, as the blended nature of the electrode creates a new paradigm, with the Si/Gr ratio likely changing with aging. Although *ex-situ* techniques have been used, a set of ~~*in-*~~*operando* tools that enable diagnosis and prognosis on this technology has yet to be developed. Herein, we present a mechanistic investigation that generates a complete degradation mapping coupled with proposed aging features of interest, to attain accurate diagnosis and prognosis. The mechanistic model allows ~~the visualization of~~ analyzing aging modes that display~~s~~ incubation periods as a potential prelude to thermodynamic plating, and the identification via incremental capacity of unique silicon features that change predictably as it degrades. A comprehensive look-up table summarizing key features is provided to provide support both to scientists and engineers on designing next-generation battery management systems for this technology.

Keywords

Silicon-graphite; Nickel-rich, NMC 811; Incremental capacity; Mechanistic model simulations; Battery degradation mapping;

1. Introduction

Lithium-ion batteries (LiB) performance is steadily improving year after year thanks to the advancement of manufacturing processes and to the introduction of superior electrode materials [1–3]. Among the most promising new materials recently introduced are silicon-graphite (Si-Gr) negative electrodes (NE) and nickel-rich nickel manganese cobalt oxide $LiNi_{0.8}Mn_{0.1}Co_{0.1}O_2$ (NMC_{811}) positive electrodes (PE) [4,5].

Energy-dense Si-Gr blended NE, are recognized as one of today's most promising battery technologies capable of meeting the ever-increasing requirements of LiB systems. Although the preliminary research stage of Si-based anodes dates back to the late 1990s [6,7], its market introduction is very recent due to the performance and reliability issues found throughout its development stages [4]. Nowadays, the issues that hampered Si-based anodes cyclability – mainly, large volumetric changes and subsequent solid-electrolyte interphase (SEI) formation – have been partly addressed by using several approaches, [8–12] one of which being the use of blended electrodes containing silicon and graphite [13–15]. To take full advantage of the NE increase of energy, the PE should also exhibit high capacity. This desired capacity can be attained using nickel-rich materials [5,16–18]. In particular, $LiNi_{0.8}Mn_{0.1}Co_{0.1}O_2$ (NMC_{811}) is currently used in last-generation commercial Si–Gr based cells [19,20]. In total, due to these technological advances, today's commercial 18650 batteries with Si-Gr/NMC_{811} configuration exhibit capacities as high as 3.5 Ah, with the Si accounting just for 3 to 4% of the electrode weight [19–21].

Recent studies on Si-based anodes have been focused on understanding the complexity of the degradation phenomena from a material science perspective [20,22–24]. As shown, the underpinning degradation of Si-based anodes has been attributed by unstable SEI and severe volumetric changes of over 300% that lead to particle cracking and electrical isolation [15]. These degradation phenomena correspond to the aging modes loss of lithium inventory (LLI)

and loss of active material (LAM), respectively [25]. Despite the valuable insights attained in those studies, their methodology (based on *ex-situ*, surface-science advanced techniques) is not applicable for direct use in battery management systems (BMS), which require non-invasive techniques. This issue is becoming a critical aspect that needs to be addressed, as these new battery technologies are emerging and are expected to be deployed in consumer electronics and next-generation electric vehicles (EVs) [26,27].

In this study, we adapted the non-invasive battery diagnosis and prognosis mechanistic framework to Si-Gr/NMC_{811} batteries. The use of mechanistic models to attain diagnosis and prognosis on battery performance has been demonstrated to be effective for most current technologies [28–31], but is yet to be developed for the Si-Gr/NMC_{811} configuration. In particular, the use of a blended material (i.e., Si-Gr) on the NE creates a new paradigm, since silicon is likely to age independently and at faster rates than graphite, all within the same electrode [21,23,32]. Hence, aging modes LLI, and LAM on graphite and on silicon, can take place at different rates due to the blended nature of the electrode. This phenomenon adds an additional complexity level to accurate diagnoses that was never investigated before. Although studies on blended PE were undertaken [33–35], herein, we introduce for the first time the emulation of a blended NE to properly address each active material from an individual perspective. We further expand in more detail the model construction, so it can be applied to either PE or NE blended materials. By combining the knowledge of our established mechanistic approaches with the information obtained from stand-alone Si-based experiments, the fractional degradation of each blended material can be estimated. We also present for the first time the degradation mapping of this cell technology, together with the main features of interest (FOIs) to enable proper sensibility analysis [30,36] and to facilitate future degradation studies on commercial Si-Gr/NMC_{811} systems. The knowledge gained from this study shall help to further understand degradation of commercial Si–Gr batteries with the use of non-invasive,

in-situ techniques, which can be applied for the development of accurate, next-generation BMSs.

2. Experimental

Electrochemical characterizations

To develop an accurate full-cell reconstruction for implementation in the mechanistic model, four electrode datasets are needed. This includes the harvested PE and NE from a Si-based commercial cell, in this case NMC_{811} vs. Li and Si-Gr vs. Li, together with graphite vs. Li and silicon vs. Li. to reconstruct the blended anode.

For this study, 55 INR18650-35E cells from Samsung-SDI were purchased from an online vendor. According to the manufacturer, this cell exhibits a standard discharge capacity ≥ 3,350 mAh, when discharged at C/1 within the voltage limits (4.2 V charge, 2.65 V cut-off). In this work, a representative cell was subjected to a set of standard conditioning tests [28], including tests at C/25. A multichannel, high-precision series Arbin LBT was used for testing. The cell was placed at constant 23 °C in a Memmert environmental chamber.

This representative cell was later disassembled to harvest the PE and NE. Standard operation procedures (SOPs) were followed for cell disassembling and half-cell construction, as discussed in Ref. [37]. These SOPs were developed based on previous works [38,39], our laboratory experience [31,37,40] and recent recommendations on the topic [41,42] to ensure truthful experimental data, a critical factor to attain accuracy in the half-cell reconstruction and the quantification of the degradation effects. The standard Gr vs. Li dataset was taken from the *'alawa* [43] database library of electrodes, whereas the Si vs. Li dataset was taken from Ref. [44].

Non-electrochemical characterizations

Additional characterization, including scanning electron microscopy (SEM) with energy-dispersive x-ray spectroscopy (EDX) as well as X-ray diffraction (XRD), were carried out to validate electrode composition.

SEM and EDX were carried out using the Helios Nanolab 660 DualBeam FIB-SEM (FEI, now Thermo Fisher Scientific) at the Advanced Electron Microscopy Center at the University of Hawai'i at Mānoa.

Powder diffraction data was collected at the X-ray Atlas lab at the Hawai'i Institute of Geophysics and Planetology, using a Bruker D8 Advance high resolution powder diffractometer, equipped with 2kW CuKa X-ray source and LYNXEYE XE detector. The source was configured in the Bragg-Brentano parafocusing geometry. The data was collected using standard sample mount, in a theta-2 theta mode, with spinning the sample around the phi goniometer axis at 15 revolutions per minute. The scanning range was 5 to 85 deg, with a step on 0.02 and 0.5 s exposure per step. The data was analyzed using DIffrac.Eva software.

Simulation tests

Computer simulations were undertaken using the *'alawa* battery diagnosis and prognosis toolbox, developed at the University of Hawai'i [43]. The toolbox used the model described in detail in Ref. [25].

3. Results

3.1. Half-cell experimental data

Half-cell experiments are essential to build a virtual replicate of the full cell and construct the mechanistic model. Fig. 1 is the half-cell data voltage profiles and the associated incremental capacity (IC) signature for a C/25 charge of the harvested PE (Fig. 1a,b), and NE (Fig. 1d,e).

The harvested PE IC curve (Fig. 1b) presented four distinctive redox peaks (noted ①-④) located at ~3.6 V, 3.7 V, 4 V and 4.2 V, which corresponds to the unique signature of Ni-rich NMC_{811} [16]. This material was further analyzed by XRD and EDX, confirming the dominance of nickel (Supplementary material Fig. S5).

For the harvested NE, the IC curves exhibit six peaks (Fig. 1d,e, black curves). Peaks ❶ to ❺ can be attributed to Gr (cf. Fig. 1d,e, red curves) [45], whereas a distinctive peak ❻ appeared at a higher potential of ~0.45 V. This peak can be attributed to Si (cf. Fig. 1d,e, gold curves for standard micro-porous Si signature). The standard Gr and the harvested NE profiles are proportional within a potential window below ~0.23 V (see Fig. 2d, red and black, respectively). Above that potential, the harvested NE shows noticeable differences, including the appearance of an additional plateau, showcasing the characteristics of Si-Gr blended electrodes, as shown by Yao et al. [22], and confirmed with the electrochemical profile of standard micro-porous Si vs. Li (Fig. 1d,e, gold color). The delithiation process is shown to reveal the characteristic high potential peak *ca.* 0.45–0.49 V that created peak ❻ in the harvested, Si-Gr electrode (Fig. 1d,e, black curve). During delithiation, Li^+ ion extraction occurs first from graphite particles that fully delithiate within the 0.01–0.23 V range, then from Si within the 0.23–1.0 V range [22,23,32], a phenomenon observed in Fig. 1d (black curve). It is well known that the (de-)lithiation of Si electrodes show large potential hysteresis, together with less pronounced plateaus [23,46,47], while standard graphite shows comparatively minor hysteresis and plateau changes. Supplementary material presents representative charge/discharge profile curves (Figs. S1-S2) for the four constructed half-cells and the experimental full cell (Figs. S3). In addition to the electrochemical tests, EDX mapping showed the intermingled nature of the negative electrode with two sets of grains of different morphologies (see Supplementary material Fig. S4). The above results confirmed that the NE is a blended Si-Gr electrode. The graphite grains are in the 20 µm range, whereas the Si grains are in the 5-10 µm range, as shown in Fig. 2c,f. EDX analysis calculated a Si content of ~3-4

wt% on the harvested NE (see Supplementary material Fig. S4), which is in concordance literature on equivalent cell chemistry and cell format commercial Si-Gr batteries [20,21].

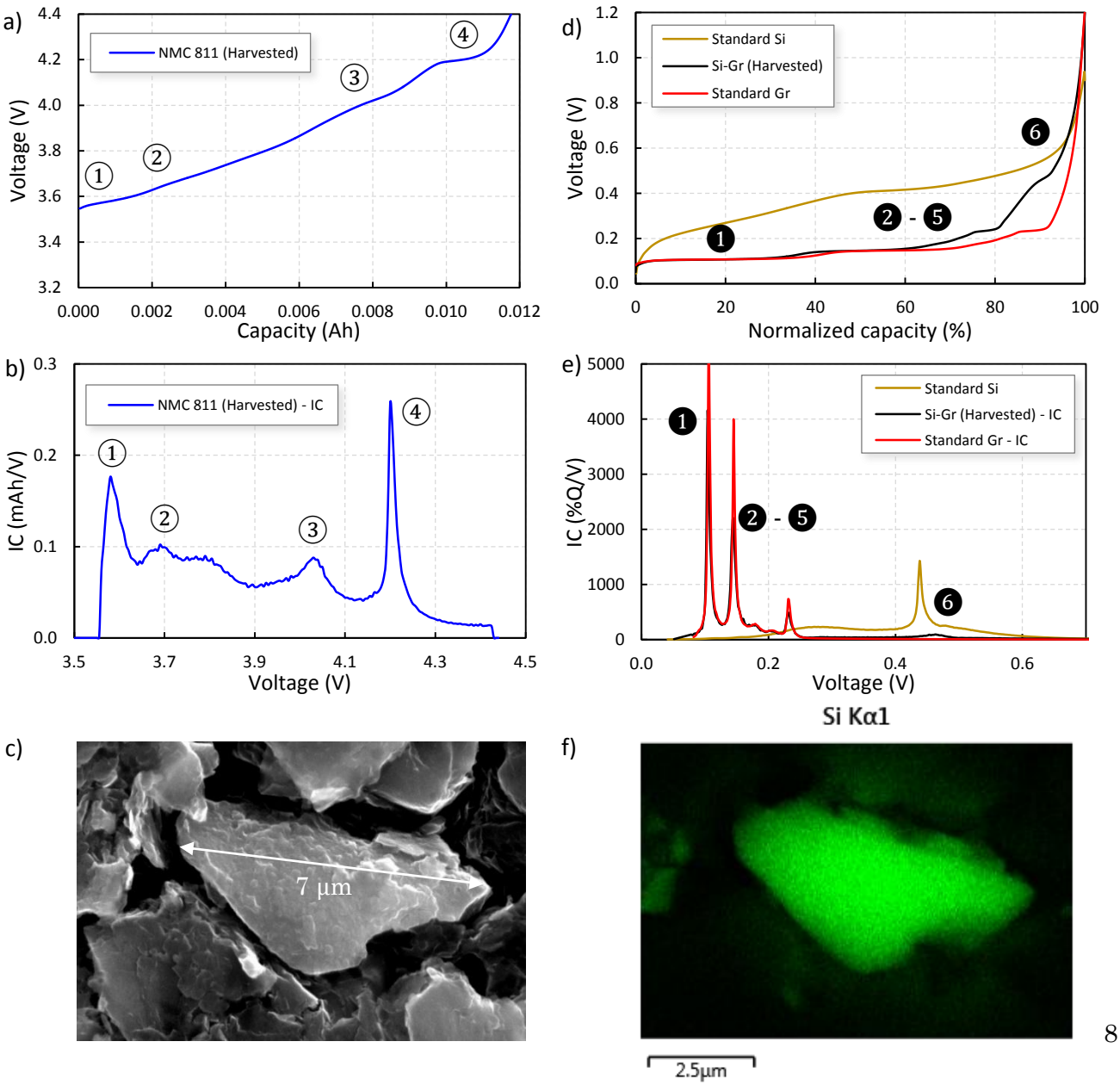

Fig. 1. (a) Voltage profile of harvested NMC_{811} vs. Li and (b) corresponding IC curves. (d) and (e) show the voltage and IC signatures for half-cell harvested Si-Gr (black), standard Gr (red) and porous Si (gold). All were cycled vs. Li. (c) and (f) show SEM images at high magnification of the fresh Si-Gr anode, where the bright grain is silicon (f)

3.2. Emulations and full-cell reconstruction

For the full-cell emulation process, a virtual mechanistic reconstruction that behaves as close as possible to the commercial cell is required. The full-cell reconstruction is to be accomplished in three steps; (i) reconstruct the harvested blended NE, (ii) reconstruct the full cell, both with the reconstructed NE and the harvested PE, and (iii), fine-tune kinetic adjustments to accurately match the experimental cell kinetics. In step (i), the reconstruction of the blended NE is attained by determining the capacity contributions of the individual standard micro-porous Si and standard Gr electrodes (i.e., %Gr + %Si). The obtained reconstructed NE shall match the signature of the harvested NE. In step (ii), the full cell is constructed from the combination of reconstructed NE and the harvested PE. Here, the loading ratio (LR) and offset (OFS) [25,37] are the parameters that are adjusted to obtain a reconstruction of the experimental full-cell data. To complete the emulation model (step iii), fine-tune kinetic adjustments are carried out. This is required as experimental full-cell differs from the reconstructed mechanistic model due to several kinetic-related phenomena [48]. The mechanistic model is obtained from half-cell electrode testing vs. Li, while the full-cell configuration internally combines its working electrodes, which introduces differences in cell pressure, separator and electrolyte composition [41,42]. Hence, adjustments to the kinetics parameters of the reconstructed model are necessary. All the above steps and parameter modifications can be performed in the '*alawa* toolbox.

Fig. 2a-b compares the voltage profiles and IC curves, respectively, of the harvested NE with the '*alawa* emulated blended Si-Gr NEs with the Si contribution varied from 0% to 40% of the

total NE capacity. It is observed that increasing the Si capacity ratio in the blended electrode produces significant changes, particularly on its characteristic high voltage peak ❻. Using peak ❻ as the main feature for comparison with the harvested electrode (Fig. 2b, inset figure), an estimation of the capacity contribution of 10% of Si and 90% of Gr was obtained. This estimation corroborates with EDX results since Si provides more capacity per weight than Gr. These capacity ratios are also in good agreement with those found in the literature on equivalent cell chemistry and cell format [19,21]. The slight shape difference between reconstructed and harvested NE observed on peak ❻ (Fig. 2b, inset) is to be modified on the last full-cell adjustment stage by accounting for the difference in electrode kinetics.

Fig. 2c presents the final cell reconstruction, where the IC curves of the experimental full cell (gray) are compared versus the reconstructed full-cell model (green), showing good agreement between the two. Peak numbering corresponds to the convolution of the NE (circled, black) with the PE (circled, white). The cell reconstruction parameters that best match the experimental cell were a LR of 0.9 between the NE and the PE and an OFS of 10%. These cell parameters match with values from literature on cells with equivalent chemistries and formats [19,21]. A kinetic modification of 0.1 on the reconstructed NE was found to be the best value to match with the experimental cell (Fig. 2c, inset figure) [25,48].

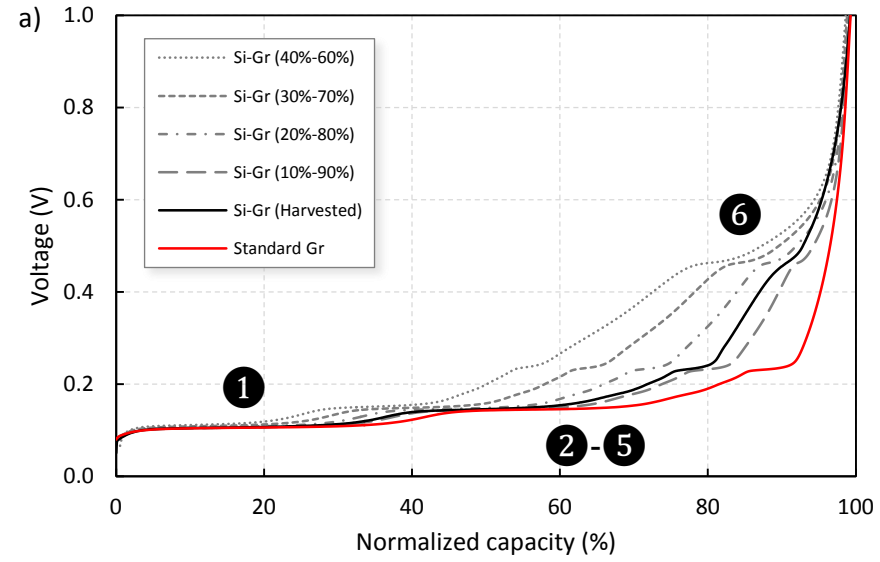
a)
Si-Gr (40%-60%)
Si-Gr (30%-70%)
Si-Gr (20%-80%)
Si-Gr (10%-90%)
Si-Gr (Harvested)
Standard Gr
Voltage (V)
Normalized capacity (%)
1
2 - 5
6

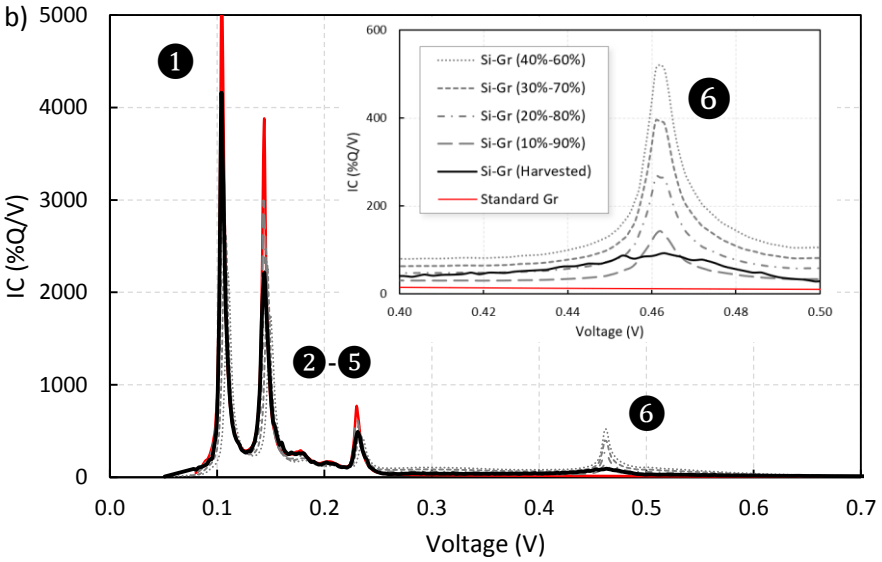
b)
IC (%Q/V)
Voltage (V)
1
2 - 5
6
Si-Gr (40%-60%)
Si-Gr (30%-70%)
Si-Gr (20%-80%)
Si-Gr (10%-90%)
Si-Gr (Harvested)
Standard Gr

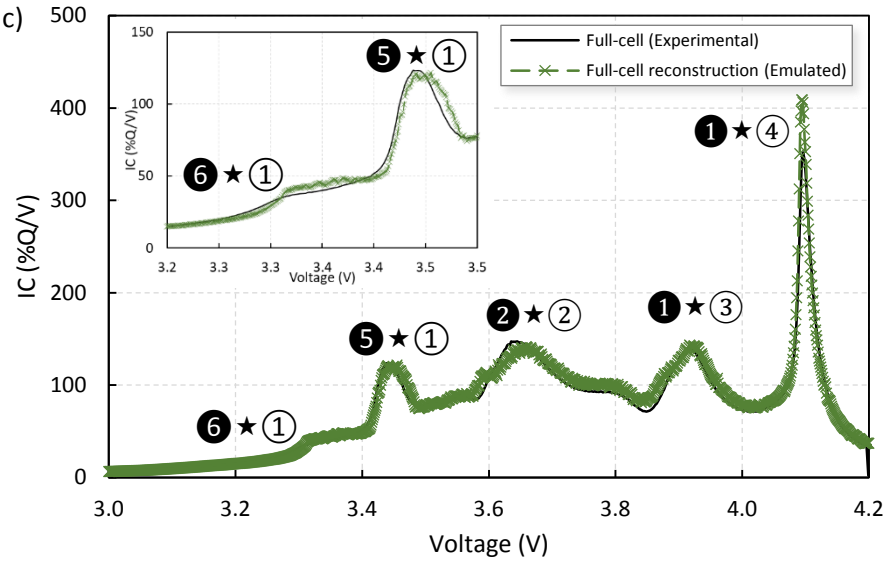

Fig. 2. (a) Voltage profile and (b) its corresponding IC curves, for standard Gr (red), harvested Si-Gr (black), and emulated Si-Gr (gray) with Si capacity contribution varied from 0% to 40%. Inset image in (b) shows the significant differences of the emulated blended (gray) on voltage peak ❻. (c) Compares the IC curves at C/25 for experimental full cell data (black) and for the emulated reconstructed full cell (green, markers), showing on inset figure details of the kinetic adjustments results

4. Discussion

With the emulated cell defined in Fig. 2c, it is possible to simulate the degradation map of this Si-Gr/NMC_{811} cell at certain degradation rates ~~at C/25 for this Si-Gr/NMC_{811} cell~~ to reach 10% capacity loss, Fig. 3. The IC curves are shown during charge due to better on-board controllability in charger systems, and because the charging process renders each IC peak accurate presence because of more pronounced plateaus [23,46,47]. Low-rate degradation can be described with three degradation modes, the loss of lithium inventory (LLI, Fig. 3a), the loss of active material (LAM) on the delithiated (de) PE (Fig. 3b) and LAM on NE (Fig. 3d,f). In addition, concurrent loss of lithium and LAM will be referred as liPE (Fig. 3c) and liNE (Fig. 3e,g) for the PE and NE, respectively. In this work, since the negative electrode is blended, LAM on Gr (Fig. 3d,e) and on Si (Fig. 3f,g) were distinguished. The approach described here, although specifically focused on Si-Gr blended NE can be generalized to other blended materials.

In case of degradation from only LLI, Fig. 3a and from left to right, peaks ❻★① and ❺★① are shifting towards higher potentials, peak ❷★② is disappearing, peak ❶★③ is shifting towards lower potentials and peak ❶★④ intensity is slightly increasing. In case of degradation from LAM_{deNMC} (Fig. 3b), peaks ❻★①, ❺★① and ❷★② are shifting towards lower potentials while the intensity of peaks ❺★① is increasing. The peak intensities of ❶★③ and ❶★④are decreasing. In the case of LAM_{deGr} (Fig. 3d), peak ❻★① is unaffected, peak ❺★① is shrinking towards lower potentials, peak ❷★② is shifting towards lower potentials, peak ❶★③ intensity is slightly increasing and peak ❶★④ intensity is significantly decreasing. For LAM_{deSi} (Fig. 3f), peak ❻★① is shrinking towards higher potentials, peaks ❺★①, ❷★② and ❶★③ are shifting towards lower potentials, and peak ❶★④ is shrinking towards higher potentials. The lithiated losses (Fig. 3c,e, and g) are amalgams of the signatures of LLI and the corresponding non-lithiated loss with some changes cancelling each other. In case of LAM_{liNMC} (Fig. 3c), peak ❻★① is unaffected, peaks ❺★①, ❷★② and ❶★③ are shrinking towards higher potentials, and peak ❶★④ is shrinking slightly towards lower potentials. For LAM_{liGr} (Fig. 3e), peak ❻★① is shrinking towards higher potentials, peaks ❺★① and ❷★② are shifting towards higher potentials, peak ❶★③ is shrinking towards higher potentials, and peak ❶★④ is unaffected. Upon LAM_{liSi} (Fig. 3g), peak ❻★① is shrinking towards higher potentials, peaks ❺★① are ❷★② are shifting towards higher potentials, and peaks ❶★③ and ❶★④ are unaffected.

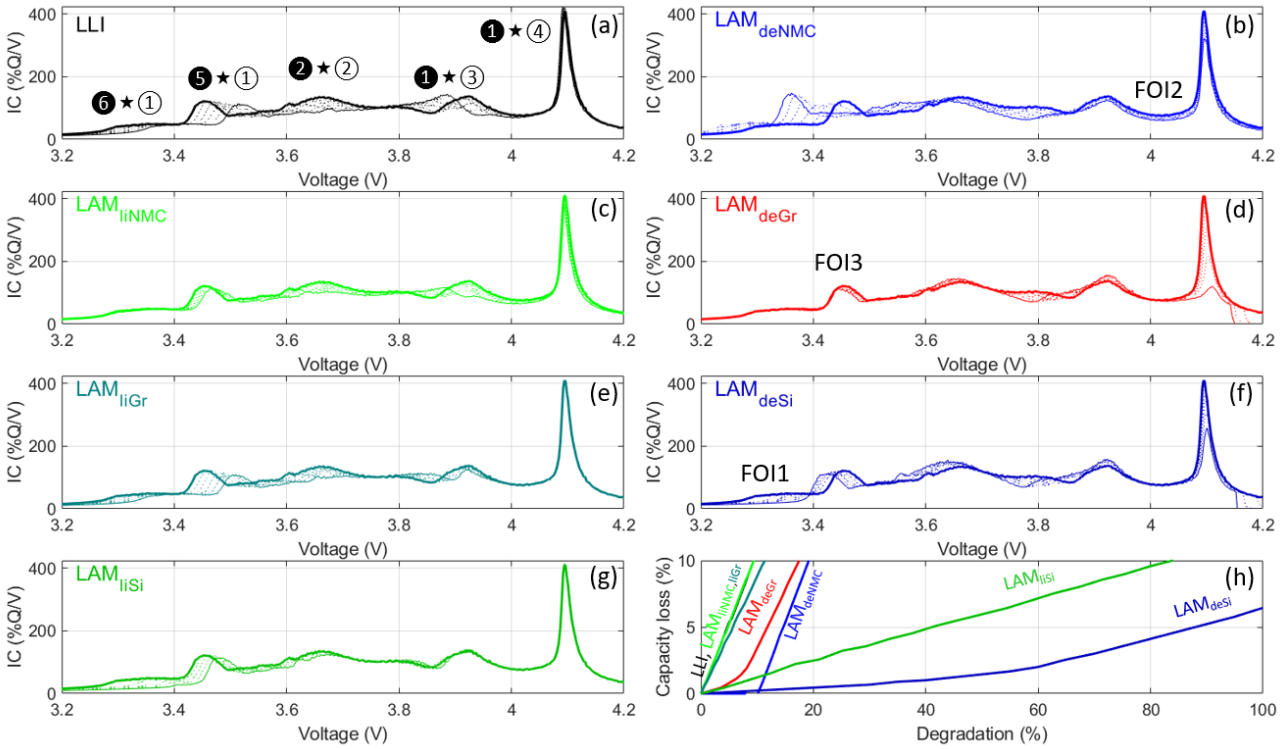

Fig. 3. Degradation map for the Si-Gr/NMC_{811} commercial cell with peak indexation and proposed FOIs. The thick lines are the initial emulated signatures, the thin lines are the emulated signatures at 10% capacity loss, and the dashed lines are the signatures at 2% intervals in between those two cases

From the degradation map, it is also possible to extract the trend in capacity loss associated with the different degradation modes, Fig. 3h. This figure provides critical information towards making a degradation mechanisms diagnosis. It is particularly effective in revealing which mode is inducing capacity loss. First of all, the capacity loss associated with degradation for LLI, LAM_{liNMC} and LAM_{liGr} are overlapping. This implies that capacity loss from these degradations are not additives and that the capacity loss is solely associated with the loss of lithium either alone (LLI) or within the active materials. Second, LAM_{deNMC}, LAM_{deGr} and LAM_{deSi} all have an incubation period in which the capacity loss is minimal despite some electrode degradation. This is induced by the positive SOC OFS that protects against LAM_{deNMC} by shifting the NE towards higher potential and by the fact that the LR is above 1 for LAM_{deGr} and LAM_{deSi} which provides a reservoir of Li ions that compensates for the LAM_{NE}. Analyzing Fig. 3e and further, for one of the LAM_{NEs} to induce capacity loss, the final voltage must go

below 4.2 V. This will lead to lithium plating. As long as peak ❶★④ is present, the capacity loss cannot be induced by some LAM_{NE}. In case of capacity loss induced by LAM_{PE}, some capacity is pushed out of the lower potential window, Fig. 3b. Therefore, if peak ❻★① is still fully in the potential window, no capacity loss can be associated with LAM_{PE}. If peak ❶★④ and peak ❻★① are both still fully in the potential window, the capacity loss can then be unambiguously associated with LLI alone.

In terms of diagnosis, some important features of interest (FOI) can also be extracted from this degradation map and the analysis of their capacity loss. First, peak ❻★①, if fully in the potential window, is only sensitive and proportional to LAM_{Si} and thus can be used to quantify that degradation mode (FOI1 on Fig. 3b). Second, if peak ❶★④ is still present, the intensity of the local minimum at its front (in charge) is a direct indicator of LAM_{deNMC} (FOI2 on Fig. 3b). Lastly, with 3 out of 4 degradation modes quantified (one from capacity loss and the others from FOI1 and 2), the position and intensity of peak ❺★①, FOI3, could be used to quantify either LLI or LAM_{Gr} by simple fitting from the simulation of the position and intensity of the peak with the three quantified parameters.

Table I is a detailed look-up table for Si-Gr/NMC811 cell technology with a summary of the changes to the main features discussed above. The look-up table provides a simple, yet reliable tool for rapid evaluation of degradation modes, avoiding extensive and complex electrochemical analyses, therefore facilitating degradation identification for BMS integration. The description of the symbols in the lookup table is as follows: vertical arrows (↓ / ↑) indicates IC peak reduction or peak increase, respectively. The horizontal arrows (→ / ←) indicates IC voltage shifts. Diagonal arrows (↙ / ↗ / ↖ / ↘) indicate a voltage shift accompanied with IC reduction or increase. Double headed arrows (↡ / ↟ / ↞ / ↠) indicate largest IC changes within the aging mode.

Table I: Look-up table of the main aging modes of the Si-Gr/NMC_{811} cell during charge

Aging modes	**Incremental Capacity Main Features** *(peak number)*					**Main features to evaluate for diagnosis and prognosis**					
	❻★①	❺★①	❷★②	❶★③	❶★④	*Features of Interest (FOI)*	*Incubation period*	*Li-plating trigger*	*Cap. fade rate*	*LR evolution*	*OFS evolution*
LLI	↠	↠	↘	←	↑	FOI 3	No	No	Fast	Unvaried	Large
LAM_{deNMC}	↞	↖	←	↓	↓	FOI 2&3	Yes	No	Medium	Increase	Large
LAM_{liNMC}	=	↘	↘	↘	↙	–	No	No	Fast	Increase	Unvaried
LAM_{deGr}	=	↙	←	↑	↡	–	Yes	Yes	Medium	Degrease	Unvaried
LAM_{liGr}	↘	↠	→	↘	=	FOI 3	No	No	Fast	Decrease	Large
LAM_{deSi}	↙	←	←	←	↡	FOI 1	Yes	Yes	Slow	Minor	Unvaried
LAM_{liSi}	↡	→	↘	=	=	FOI 1	No	No	Slow	Minor	Minor

5. Conclusion

With new electrode configurations emerging in next-generation Li-ion batteries, it is important to provide the battery research and industry community with adaptable, *in-situ* diagnosis and prognosis tools that have been proved successful in previous generation materials. We sequentially presented the framework to construct an accurate mechanistic model, from a commercial representative Si-Gr/NMC_{811} battery. The constructed model allowed us to emulate via the '*alawa* toolbox the degradation modes, including individual degradation rates of silicon and graphite within the blended negative electrode, that the battery could experience under real-life operating conditions. Both the incremental capacity curves and the full-cell capacity losses versus the degradation modes, which are required to analyze and further decipher the underpinning degradation phenomena, were presented to attain accurate battery diagnosis and prognosis analyses.

The details of the simulations allowed us to postulate that three aging modes (i.e., LAM_{deNMC}, LAM_{deGr} and LAM_{deSi}) have incubation periods. Full-cell capacity loss due to these aging modes is negligible compared to the LLI during initial cycling, but after a certain point in

aging will become considerable. In addition, the results show that both LAM_{deGr} and LAM_{deSi} modes may trigger thermodynamic plating in the cell, hence revealing a plausible impact of silicon on degradation in these blended electrodes. On the resulting IC curves, we highlight the importance of analyzing peak ❻★① as this feature directly correlates to the influence of silicon.

We set up a series of key Features of Interest (FOIs) that are sensitive to degradation and must be analyzed in detail to understand and deconvolute concurrent aging modes. As there exists a total of seven aging modes acting on four IC peaks yielding multiple possibilities of degradation, we created a look-up table that shall ease analysis of standard Si-Gr/NMC_{811} batteries. Due to the intrinsic nature of look-up tables, the features could be embedded on a microcontroller-based architecture. In a broader perspective, this paper aims to impart the capability and know-how to battery scientists and engineers, to facilitate the integration of degradation diagnosis and prognosis tools for battery management systems (BMS) operating this novel technology.

Acknowledgments

D. A. gratefully acknowledges the funding provided by the Spanish Ministry of Science and Innovation and by FEDER Grants TEC2016-80700-R (AEI/FEDER, UE) and TIN2017-84804-R, the Principality of Asturias Government under Project FC-IDI/2018/000226, and the Santander Group under Grant “Movilidad de excelencia para docentes e investigadores”. I. C. thanks the financial support by Fundación General CSIC (Programa ComFuturo). M. D. is thankful to the State of Hawai‘i and to the Asia Pacific Research Initiative for Sustainable Energy Systems (APRISES), award number # N00014-17-1-2206. The authors also would like to thank Hope Ishii, Kenta Ohtaki, and Przemyslaw Dera, and the University of Hawai‘i Material Science Consortium for Research and Education for funding the diffraction and microscopy work as well as Bernard Lestriez for the Si vs. Li data.

References

[1] N. Nitta, F. Wu, J.T. Lee, G. Yushin, Li-ion battery materials: present and future, Mater. Today. 18 (2015) 252–264. doi:10.1016/j.mattod.2014.10.040.

[2] S. Goriparti, E. Miele, F. De Angelis, E. Di Fabrizio, R. Proietti Zaccaria, C. Capiglia, Review on recent progress of nanostructured anode materials for Li-ion batteries, J. Power Sources. 257 (2014) 421–443. doi:10.1016/j.jpowsour.2013.11.103.

[3] G. Zubi, R. Dufo-López, M. Carvalho, G. Pasaoglu, The lithium-ion battery: State of the art and future perspectives, Renew. Sustain. Energy Rev. 89 (2018) 292–308. doi:10.1016/j.rser.2018.03.002.

[4] X. Zuo, J. Zhu, P. Müller-Buschbaum, Y.J. Cheng, Silicon based lithium-ion battery anodes: A chronicle perspective review, Nano Energy. 31 (2017) 113–143. doi:10.1016/j.nanoen.2016.11.013.

[5] W. Liu, P. Oh, X. Liu, M.J. Lee, W. Cho, S. Chae, Y. Kim, J. Cho, Nickel-Rich Layered Lithium Transition-Metal Oxide for High-Energy Lithium-Ion Batteries, Angew. Chemie - Int. Ed. 54 (2015) 4440–4457. doi:10.1002/anie.201409262.

[6] J.S. Xue, K. Myrtle, J.R. Dahn, An Epoxy-Silane Approach to Prepare Anode Materials for Rechargeable Lithium Ion Batteries, J. Electrochem. Soc. 142 (1995) 2927–2935. doi:10.1149/1.2048667.

[7] W. Xing, A.M. Wilson, K. Eguchi, G. Zank, J.R. Dahn, Pyrolyzed Polysiloxanes for Use as Anode Materials in Lithium-Ion Batteries, J. Electrochem. Soc. 144 (1997) 2410. doi:10.1149/1.1837828.

[8] M.T. McDowell, S.W. Lee, W.D. Nix, Y. Cui, 25th anniversary article: Understanding the lithiation of silicon and other alloying anodes for lithium-ion batteries, Adv. Mater. 25 (2013) 4966–4985. doi:10.1002/adma.201301795.

[9] C.K. Chan, H. Peng, G. Liu, K. Mcilwrath, X.F. Zhang, R.A. Huggins, Y. Cui, High-performance lithium battery anodes using silicon nanowires, Nat. Nanotechnol. 3 (2008) 31–36. doi:10.1038/nnano.2007.411.

[10] M. Gu, Y. He, J. Zheng, C. Wang, Nanoscale silicon as anode for Li-ion batteries: The fundamentals, promises, and challenges, Nano Energy. 17 (2015) 366–383. doi:10.1016/j.nanoen.2015.08.025.

[11] M.J. Choi, Y. Xiao, J.Y. Hwang, I. Belharouak, Y.K. Sun, Novel strategy to improve the Li-storage performance of micro silicon anodes, J. Power Sources. 348 (2017) 302–310. doi:10.1016/j.jpowsour.2017.03.020.

[12] M. Salah, P. Murphy, C. Hall, C. Francis, R. Kerr, M. Fabretto, Pure silicon thin-film anodes for lithium-ion batteries: A review, J. Power Sources. 414 (2019) 48–67. doi:10.1016/j.jpowsour.2018.12.068.

[13] P. Li, G. Zhao, X. Zheng, X. Xu, C. Yao, W. Sun, S.X. Dou, Recent progress on silicon-based anode materials for practical lithium-ion battery applications, Energy Storage Mater. 15 (2018) 422–446. doi:10.1016/j.ensm.2018.07.014.

[14] B. Liang, Y. Liu, Y. Xu, Silicon-based materials as high capacity anodes for next generation lithium ion batteries, J. Power Sources. 267 (2014) 469–490. doi:10.1016/j.jpowsour.2014.05.096.

[15] S. Chae, S.H. Choi, N. Kim, J. Sung, J. Cho, Integration of Graphite and Silicon Anodes for the Commercialization of High-Energy Lithium-Ion Batteries, Angew. Chemie - Int. Ed. (2019) 110–135. doi:10.1002/anie.201902085.

[16] H.J. Noh, S. Youn, C.S. Yoon, Y.K. Sun, Comparison of the structural and electrochemical properties of layered Li[NixCoyMnz]O2 (x = 1/3, 0.5, 0.6, 0.7, 0.8 and 0.85) cathode material for lithium-ion batteries, J. Power Sources. 233 (2013) 121–130. doi:10.1016/j.jpowsour.2013.01.063.

[17] Y. Xia, J. Zheng, C. Wang, M. Gu, Designing principle for Ni-rich cathode materials with high energy density for practical applications, Nano Energy. 49 (2018) 434–452. doi:10.1016/j.nanoen.2018.04.062.

[18] A. Manthiram, B. Song, W. Li, A perspective on nickel-rich layered oxide cathodes for lithium-ion batteries, Energy Storage Mater. 6 (2017) 125–139. doi:10.1016/j.ensm.2016.10.007.

[19] J. Sturm, A. Rheinfeld, I. Zilberman, F.B. Spingler, S. Kosch, F. Frie, A. Jossen, Modeling and simulation of inhomogeneities in a 18650 nickel-rich, silicon-graphite lithium-ion cell during fast charging, J. Power Sources. 412 (2019) 204–223. doi:10.1016/j.jpowsour.2018.11.043.

[20] X. Li, A.M. Colclasure, D.P. Finegan, D. Ren, Y. Shi, X. Feng, L. Cao, Y. Yang, K. Smith, Degradation mechanisms of high capacity 18650 cells containing Si-graphite anode and nickel-rich NMC cathode, Electrochim. Acta. 297 (2019) 1109–1120. doi:10.1016/j.electacta.2018.11.194.

[21] I. Zilberman, J. Sturm, A. Jossen, Reversible self-discharge and calendar aging of 18650 nickel-rich, silicon-graphite lithium-ion cells, J. Power Sources. 425 (2019) 217–226. doi:10.1016/j.jpowsour.2019.03.109.

[22] K.P.C. Yao, J.S. Okasinski, K. Kalaga, J.D. Almer, D.P. Abraham, Operando Quantification of (De)Lithiation Behavior of Silicon-Graphite Blended Electrodes for Lithium-Ion Batteries, Adv. Energy Mater. 1803380 (2019) 1803380. doi:10.1002/aenm.201803380.

[23] M. Wetjen, D. Pritzl, R. Jung, S. Solchenbach, R. Ghadimi, H.A. Gasteiger, Differentiating the Degradation Phenomena in Silicon-Graphite Electrodes for Lithium-Ion Batteries, J. Electrochem. Soc. 164 (2017) A2840–A2852. doi:10.1149/2.1921712jes.

[24] N.P. Wagner, K. Asheim, F. Vullum-Bruer, A.M. Svensson, Performance and failure analysis of full cell lithium ion battery with LiNi0.8Co0.15Al0.05O2 and silicon electrodes, J. Power Sources. 437 (2019) 226884. doi:10.1016/j.jpowsour.2019.226884.

[25] M. Dubarry, C. Truchot, B.Y. Liaw, Synthesize battery degradation modes via a diagnostic and prognostic model, J. Power Sources. 219 (2012) 204–216. doi:10.1016/j.jpowsour.2012.07.016.

[26] R. Schmuch, R. Wagner, G. Hörpel, T. Placke, M. Winter, Performance and cost of materials for lithium-based rechargeable automotive batteries, Nat. Energy. 3 (2018) 267–278. doi:10.1038/s41560-018-0107-2.

[27] C. Martin, Driving change in the battery industry, Nat. Nanotechnol. 9 (2014) 327–328. doi:10.1038/nnano.2014.92.

[28] M. Dubarry, B.Y. Liaw, Identify capacity fading mechanism in a commercial LiFePO4 cell, J. Power Sources. 194 (2009) 541–549. doi:10.1016/j.jpowsour.2009.05.036.

[29] M. Dubarry, G. Baure, A. Devie, Durability and Reliability of EV Batteries under Electric Utility Grid Operations: Path Dependence of Battery Degradation, J. Electrochem. Soc. 165 (2018) A773–A783. doi:10.1149/2.0421805jes.

[30] M. Dubarry, M. Berecibar, A. Devie, D. Anseán, N. Omar, I. Villarreal, State of health battery estimator enabling degradation diagnosis: Model and algorithm description, J. Power Sources. 360 (2017) 59–69. doi:10.1016/j.jpowsour.2017.05.121.

[31] A. Devie, G. Baure, M. Dubarry, Intrinsic variability in the degradation of a batch of commercial 18650 lithium-ion cells, Energies. 11 (2018) 1031. doi:10.3390/en11051031.

[32] M. Klett, J.A. Gilbert, S.E. Trask, B.J. Polzin, A.N. Jansen, D.W. Dees, D.P. Abraham, Electrode Behavior RE-Visited: Monitoring Potential Windows, Capacity Loss, and Impedance Changes in $Li_{1.03}(Ni_{0.5}Co_{0.2}Mn_{0.3})_{0.97}O_2$ /Silicon-Graphite Full Cells, J. Electrochem. Soc. 163 (2016) A875–A887. doi:10.1149/2.0271606jes.

[33] M. Dubarry, C. Truchot, A. Devie, B.Y. Liaw, K. Gering, S. Sazhin, D. Jamison, C. Michelbacher, Evaluation of Commercial Lithium-Ion Cells Based on Composite Positive Electrode for Plug-In Hybrid Electric Vehicle (PHEV) Applications: IV. Over-Discharge Phenomena, J. Electrochem.

Soc. 162 (2015) A1787–A1792. doi:10.1149/2.0481509jes.

[34] K. Ando, T. Matsuda, D. Imamura, Degradation diagnosis of lithium-ion batteries with a LiNi0.5Co0.2Mn0.3O2 and LiMn2O4 blended cathode using dV/dQ curve analysis, J. Power Sources. 390 (2018) 278–285. doi:10.1016/j.jpowsour.2018.04.043.

[35] G. Baure, A. Devie, M. Dubarry, Battery Durability and Reliability under Electric Utility Grid Operations: Path Dependence of Battery Degradation, J. Electrochem. Soc. 166 (2019) A1991–A2001. doi:10.1149/2.0971910jes.

[36] M. Dubarry, C. Pastor-Fernández, G. Baure, T.F. Yu, W.D. Widanage, J. Marco, Battery energy storage system modeling: Investigation of intrinsic cell-to-cell variations, J. Energy Storage. 23 (2019) 19–28. doi:10.1016/j.est.2019.02.016.

[37] D. Anseán, M. Dubarry, A. Devie, B.Y. Liaw, V.M. García, J.C. Viera, M. González, Fast charging technique for high power LiFePO4 batteries: A mechanistic analysis of aging, J. Power Sources. 321 (2016) 201–209. doi:10.1016/j.jpowsour.2016.04.140.

[38] D.P. Abraham, J.L. Knuth, D.W. Dees, I. Bloom, J.P. Christophersen, Performance degradation of high-power lithium-ion cells—Electrochemistry of harvested electrodes, J. Power Sources. 170 (2007) 465–475. doi:10.1016/j.jpowsour.2007.03.071.

[39] M. Kassem, C. Delacourt, Postmortem analysis of calendar-aged graphite/LiFePO4 cells, J. Power Sources. 235 (2013) 159–171. doi:10.1016/j.jpowsour.2013.01.147.

[40] A. Devie, M. Dubarry, Durability and Reliability of Electric Vehicle Batteries under Electric Utility Grid Operations. Part 1: Cell-to-Cell Variations and Preliminary Testing, Batteries. 2 (2016) 28. doi:10.3390/batteries2030028.

[41] A.U. Schmid, M. Kurka, K.P. Birke, Reproducibility of Li-ion cell reassembling processes and their influence on coin cell aging, J. Energy Storage. 24 (2019) 100732. doi:10.1016/j.est.2019.04.006.

[42] V. Murray, D.S. Hall, J.R. Dahn, A Guide to Full Coin Cell Making for Academic Researchers, J. Electrochem. Soc. 166 (2019) A329–A333. doi:10.1149/2.1171902jes.

[43] 'Alawa Central, (n.d.). https://www.soest.hawaii.edu/HNEI/alawa/ (accessed January 5, 2017).

[44] D. Mazouzi, R. Grissa, M. Paris, Z. Karkar, L. Huet, D. Guyomard, L. Roué, T. Devic, B. Lestriez, CMC-citric acid Cu(II) cross-linked binder approach to improve the electrochemical performance of Si-based electrodes, Electrochim. Acta. 304 (2019) 495–504. doi:10.1016/j.electacta.2019.03.026.

[45] J. Dahn, Phase diagram of LixC6., Phys. Rev. B. Condens. Matter. 44 (1991) 9170–9177.

[46] D.S.M. Iaboni, M.N. Obrovac, $Li_{15}Si_4$ Formation in Silicon Thin Film Negative Electrodes, J. Electrochem. Soc. 163 (2016) A255–A261. doi:10.1149/2.0551602jes.

[47] J. Luo, X. Zhao, J. Wu, H.D. Jang, H.H. Kung, J. Huang, Crumpled graphene-encapsulated Si nanoparticles for lithium ion battery anodes, J. Phys. Chem. Lett. 3 (2012) 1824–1829. doi:10.1021/jz3006892.

[48] S. Schindler, G. Baure, M.A. Danzer, M. Dubarry, Kinetics accommodation in Li-ion mechanistic modeling, J. Power Sources. 440 (2019) 227117. doi:10.1016/j.jpowsour.2019.227117.

Table(s) - provided separately

Aging modes	**Incremental Capacity Main Features** *(peak number)*					**Main features to evaluate for diagnosis and prognosis**					
	❻★①	❺★①	❷★②	❶★③	❶★④	*Features of Interest (FOI)*	*Incubation period*	*Li-plating trigger*	*Cap. fade rate*	*LR evolution*	*OFS evolution*
LLI	↠	↠	↘	←	↑	FOI 3	No	No	Fast	Unvaried	Large
LAM$_{deNMC}$	↞	↖	←	↓	↓	FOI 2&3	Yes	No	Medium	Increase	Large
LAM$_{liNMC}$	=	↘	↘	↘	↙	–	No	No	Fast	Increase	Unvaried
LAM$_{deGr}$	=	↙	←	↑	↡	–	Yes	Yes	Medium	Degrease	Unvaried
LAM$_{liGr}$	↘	↠	→	↘	=	FOI 3	No	No	Fast	Decrease	Large
LAM$_{deSi}$	↙	←	←	←	↡	FOI 1	Yes	Yes	Slow	Minor	Unvaried
LAM$_{liSi}$	↡	→	↘	=	=	FOI 1	No	No	Slow	Minor	Minor

Figure(s) - provided separately

Click here to download Figure(s) - provided separately: Fig. 1.docx

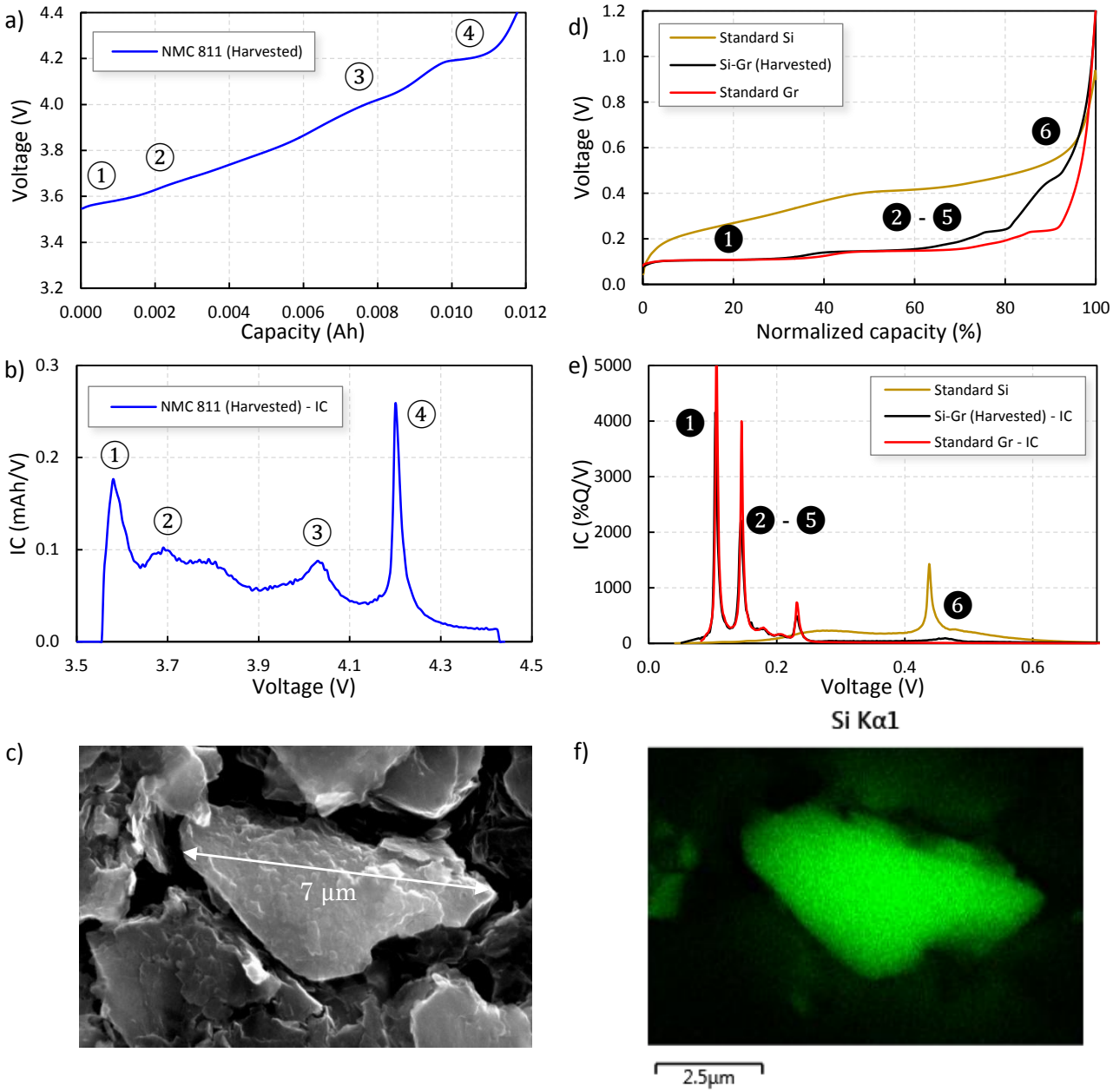

Figure(s) - provided separately

Click here to download Figure(s) - provided separately: Fig. 2.docx

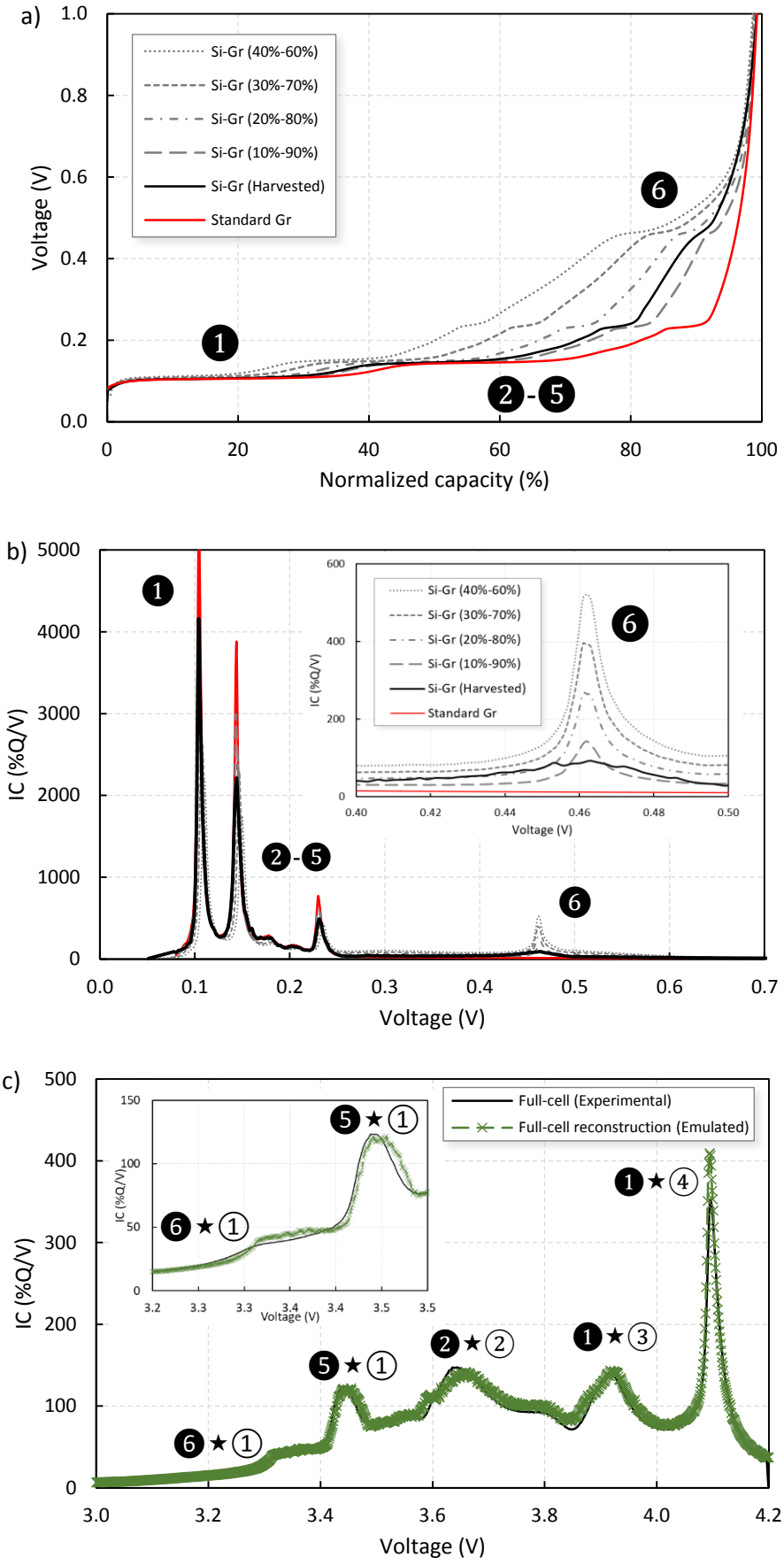

Figure(s) - provided separately

Click here to download Figure(s) - provided separately: Fig. 3 - Revised.docx

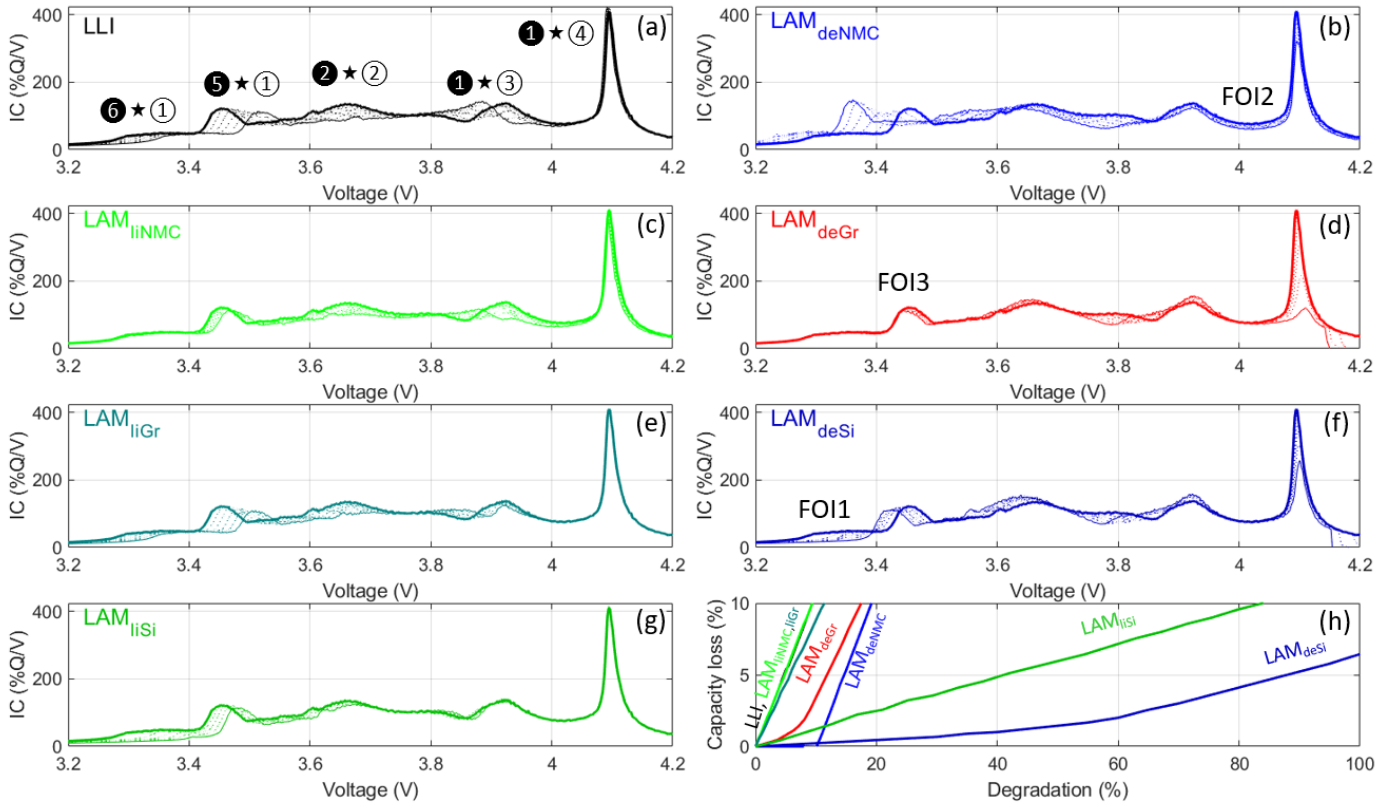

Fig. 1. (a) Voltage profile of harvested NMC_{811} vs. Li and (b) corresponding IC curves. (d) and (e) show the voltage and IC signatures for half-cell harvested Si-Gr (black), standard Gr (red) and porous Si (gold). All were cycled vs. Li. (c) and (f) show at high magnification SEM images of the fresh Si-Gr anode, where the bright grain is silicon (f)

Fig. 2. (a) Voltage profile and (b) its corresponding IC curves, for standard Gr (red), harvested Si-Gr (black), and emulated Si-Gr (gray) with Si capacity contribution varied from 0% to 40%. Inset image in (b) shows the significant differences of the emulated blended (gray) on voltage peak ❻. (c) Compares the IC curves at C/25 for experimental full cell data (black) and for the emulated reconstructed full cell (green, markers), showing on inset figure details of the kinetic adjustments results

Fig. 3. Degradation map for the Si-Gr/NMC_{811} commercial cell with peak indexation and proposed FOIs. The thick lines are the initial emulated signatures, the thin lines are the emulated signatures at 10% capacity loss, and the dashed lines are the signatures at 2% intervals in between those two cases

Table I: Look-up table of the main aging modes of the Si-Gr/NMC_{811} cell during charge

Supplementary Materials

Click here to download Supplementary Materials: Supplementary Material - Revised.docx